CHAPTER 4: A PATH TRACING AND DEFORMITY ESTIMATION METHODOLOGY FOR REGISTRATION OF THORACIC CT IMAGE SEQUENCES

The chapter presents a methodology which involves an automatic registration process for tracing deformity paths of the thoracic region between full inhale and exhale positions based on Hessian-matrix based feature detector and Haar wavelets based descriptor along with Optical Flow Motion (OFM) estimation based point tracker technique. The proposed work presents a unique and innovative arrangement of methods to compute the average deformation of the thoracic region from all anatomical positions. Often clinical studies on image based respiratory systems either suffer road blocks or yield inconsistent results due to artifacts from a variety of subjects' erratic breathing patterns. This leads to loss of resources and time to ultimately get inconclusive and potentially wrong results. This work can be seen as an automatic way of computing average thoracic deformation for a set of diverse subjects. In an image sequence, corresponding control point pairs or landmarks can be used to define the internal deformations with respect to time, point of view or modality. Defining enough number of control points in a thoracic image temporal sequence to describe the deformations happening in it is a tedious task. This inspired the use of automatic definition of control points in the proposed work. The credibility and performance of the above proposed method is demonstrated by its exemplary experimental results.

The proposed methodology registers consecutive, equidistant frames in a temporal, thoracic CT image sequence starting from full inhale to full exhale positions by assessing the transformations happening in the image over time for a

group of test subjects through all three anatomical positions (APs). The sequences are such that the first and last frames of a sequence are the most deformed frames with respect to each other i.e. first frame is the full inhale frame and the last one is the full exhale frame. The number of these frames depends upon the time gap considered between acquiring of these frames. Larger the time gap, lesser would be the number of frames in the sequence from start to finish. These frames are compared and contrasted against each other to find common landmark set of points between them. They would be same points in different frames at different (may be) coordinate locations. These points serve as input to an OFM estimation based point tracking algorithm which would track a point from the first temporal frame up until the last frame in the sequence it appears in, (few points were not found to carry through all the frames from start to finish (as we later found out in the process)). This process is completed for remaining points in the common landmark point set throughout the sequence. One of the frames is considered as a 'base' or 'reference' and rest of the frames are registered with respect to the reference/base. In the proposed method, the full inhale frame which is the first one has been considered as the reference frame as a default for all subjects through all APs. The distances each point cover between temporally ordered frames of the sequence from its starting frame to the last frame it is observed in is estimated using its coordinate values in those respectively ordered frames. Average translation values are calculated for the point set for all test subjects through all three APs. These point set average translations summed up over the complete sequence give an estimation of the deformations happened from first to last frame of the temporal image sequence. Each point in the common landmark point cloud has been traced through frames and optical flow determined for it.

4.1 Introduction

Accounting for organ motion in image based lung cancer radiation treatment is considered as an important challenge in medical imaging [Goitein, M., 2004]. Lung deformations have been constant focus of studies for the verification of medical imaging equipments and for medical training purposes for a long period of time and still, physiologically speaking, very little is understood about the respiratory movement [Stevo, N. *et al.*, 2009]. The movement of the lung is passive; a result of the movement of other parts of the body, such as the diaphragm and the thoracic cage, and it is not possible to observe the lung directly, as it would collapse if the thoracic cage is opened. The clinical relevance of this research is diverse. Respiratory motion is related to the function of the lung and therefore a diagnostic value in itself [Ehrhardt, J. *et al.*, 2011]. Furthermore, breathing induced organ motion potentially leads to image artifacts and to position uncertainty in image guided procedures. Particularly in radiotherapy planning of thoracic and abdominal tumors, the respiratory motion causes important uncertainties and is a significant source of error [Keall, P. J. *et al.*, 2006]. Therefore, there has been a large and continuing growth in studies and applications of 4D CT images for motion measurement, radiotherapy treatment planning, as well as functional investigations [Reinhardt, J. M. *et al.*, 2008]. "A non-invasive method to describe lung deformations was proposed using NURBS surfaces based on imaging data from CT scans of actual patients" [Stevo, N. *et al.*, 2009; Tsui, B. M. W. *et al.*, 2000]. V. B. Zordan and associates created an anatomical inspired, physically based model of human torso for the visual simulation of respiration [Zordan, V. B. *et al.*, 2004]. It has been shown that breathing motion is not a robust and 100% reproducible process [Nehmeh, S. A. *et*

al., 2004; Vedam, S. S. *et al.*, 2004] and now there is a widespread common consent that it would be useful to use prior knowledge of respiratory organ motion and its "variability to improve radiotherapy planning and treatment delivery" [Blackall, J. M. *et al.*, 2006].

The framework that has been acquired in this article is that the constituents of a thoracic image sequence with starting frame as the full inhale and ending frame as the full exhale are compared to find a set of common feature points, only distinction in them being different coordinate values (may be) and that they exist in different temporal frames. These common feature points are collectively called as the corresponding feature set. This feature set then serves as input to an OFM estimation algorithm as control point cloud corresponding to the thoracic image sequence. The estimation algorithm then traces the deformation in the thoracic image sequence right through initial to final frame.

The role of image registration techniques is increasing in these applications. Image registration enables the estimation of the breathing-induced motion and the description of the temporal change in position and shape of the structures of interest by establishing the correspondence between images acquired at different phases of the breathing cycle. A variety of image registration approaches have been used for respiratory motion estimation in recent years [Sarrut, D. *et al.*, 2006]. Image Registration is the alignment/overlaying of two or more images so that the best superimposition can be achieved. These images can be of the same subject at different points in time, from different viewpoints or by different sensors. This way the contents from all the images in question can be integrated to provide richer information. It helps in understanding and thus reducing the differences occurred due to variable imaging conditions. Most

common applications of Image Registration include remote sensing (integrating information for GIS), combining data obtained from a variety of imaging modalities (combining a CT and an MRI view of the same patient) to get more information about the disease at once, cartography, image restoration etc. An image registration method targets to find the optimal transformation that aligns the images in the best way possible. If the underlying transformation model allows local deformations, i.e. nonlinear fields' u(x), then it is called Deformable Image Registration (DIR) [Muenzing, S. E. A. *et al.*, 2014].

Image registration has been categorized into two kinds based on the type of image it is being applied for. The two kinds of images are Rigid Images and Deformable Images. Rigid images are those of structures with rigid morphological properties e.g. bones, buildings, geographical structures etc. Deformable images are those of structures shape and size of which can be modeled after tangible physically deformable models [Sotiras, A. *et al.*, 2013]. Rigid image registration although is an important aspect of registration it is not the topic of discussion in this article. Since the discussion is about Medical Image Registration and almost all anatomical parts or organs of the human body are deformable structures, the concentration here is on DIR [Oliviera, F. P. M. & Tavares, J. M. R. S., 2012].

One of the three basic categories of physical models [Modersitzki, J., 2004] conceptually utilized in this article is the Diffusion models. Thirion, inspired by Maxwell's Demons [Thomson, W. 1874], proposed to perform image matching as a diffusion process, his work in turn inspired most of the work done in image registration using diffusion models [Thirion, J. P., 1998]. J. M. Peyrat & associates used multi-channel Demons to register time-series of cardiac images by enforcing trajectory constraints [Peyrat, J. M. *et al.*, 2008]. Each time instance

was considered as a different channel while the estimated transformation between successive channels was considered as constraint. B. T. T. Yeo and associates [Yeo, B. T. T. *et al.*, 2010] derived Demons forces from the squared difference between each element of the Log-Euclidean transformed tensors while taking into account the reorientation introduced by the transformation.

A safer and more accurate evaluation of the respiratory movement will help in the selection of the appropriate medicine, the determination of the effectiveness of a treatment, to reduce the number of cases of clinical trial, observe the progress of rehabilitation treatments, among other possible applications. The present work uses a novel and never-tried-before automatic approach for deformity estimation in a temporal sequence of thoracic CT images.

4.2 Background

The background study of this chapter includes detailed discussion of prominent works and algorithms studied in the process of proposition of this method. The algorithms and earlier proposed methods under discussion are categorically ordered keeping in mind their acute relevance and year of occurrence/proposition/publication to the scientific community. Propositions occurring at a later instant in timeline are given higher priority in discussion in comparison to earlier works to establish better context. These methods are compared in a tabular format in table C.1 in Appendix C.

D. Sarrut and associates [Sarrut, D. *et al.*, 2006] proposed to "simulate an artificial four-dimensional (4-D) CT image of the thorax during breathing". It was performed by deformable registration of two CT scans acquired at inhale and exhale breath-hold. Breath-hold images were acquired with the ABC (Active

Breathing Coordinator) system. Dense deformable registrations were performed. The method was a minimization of the sum of squared differences (SSD) using an approximated second-order gradient. Gaussian and linear-elastic vector field regularizations were compared. A new preprocessing step, called a priori lung density modification (APLDM), was proposed to take into account lung density changes due to inspiration. It consisted of modulating the lung densities in one image according to the densities in the other, in order to make them comparable. Simulated 4-D images were then built by vector field interpolation and image re-sampling of the two initial CT images. A variation in the lung density was taken into account to generate intermediate artificial CT images. The Jacobian of the deformation was used to compute voxel values in Hounsfield units. The accuracy of the deformable registration was assessed by the spatial correspondence of anatomic landmarks located by experts. APLDM produced statistically significantly better results than the reference method (registration without APLDM preprocessing). The mean ±standard deviation of distances between automatically found landmark positions and landmarks set by experts were 2.7±1.1 mm with APLDM, and 6.3±3.8 mm without. Inter-expert variability was 2.3±1.2 mm. The differences between Gaussian and linear elastic regularizations were not statistically significant. In the second experiment using 4-D images, the mean difference between automatic and manual landmark positions for intermediate CT images was 2.6±2.0 mm. The generation of 4-D CT images by deformable registration of inhale and exhale CT images was found to be feasible. This might lower the dose needed for 4-D CT acquisitions or might even help to correct 4-D acquisition artifacts. Such a 4-D CT model could be used to propagate contours, to compute a 4-D dose map, or to simulate CT acquisitions with an

irregular breathing signal. It could serve as a basis for 4-D radiation therapy planning. Despite these encouraging and fruitful projections, further work was found to be needed to make the simulation more realistic by taking into account hysteresis and more complex voxel trajectories.

N. Stevo and associates [Stevo, N. *et al.*, 2009] proposed a method for registration of temporal sequences of coronal and sagittal images obtained from magnetic resonance (MR). They suggested that for each image in coronal and sagittal MRI sequences, the information contained in the intersection segment would be determined, and the matching would be done to determine the best sagittal images for each coronal image and vice-versa. The final MR image registration would be the determination of the best images in a sequence that fits a chosen image in another sequence. One of the registration approaches used was determining the distance between the images by comparing pixel by pixel and combining these differences in a single value. The other one was Fourier Transform based, since fourier description of an edge is also used for template matching. The resulting pairs from both algorithms were different. It was noticed that both pairs have a satisfactory visual registration. The temporal sequence of images represented discrete instants in time, and such an almost perfect fitting is considered very rare. The temporal registration algorithm based on pixel by pixel comparison and Fourier transform showed several satisfactory results, however it was found not possible to overcome the temporal low rate of image acquisition. One of the future works according to the authors could be the definition of a new registration algorithm combining pixel comparison and time segmentation.

Edward Castillo and associates [Castillo, E. *et al.*, 2010] suggested a four-dimensional deformable image registration (4D DIR) algorithm, referred to as 4D

local trajectory modelling (4DLTM) and it was applied to thoracic 4D computed tomography (4DCT) image sets. The proposed method exploited the incremental continuity present in 4DCT component images to calculate a dense set of parameterized voxel trajectories through space as functions of time. The spatial accuracy of the 4DLTM algorithm was compared with an alternative registration approach in which component phase to phase (CPP) DIR is utilized to determine the full displacement between maximum inhale and exhale images. Cubic polynomials were found to provide sufficient flexibility and spatial accuracy for describing the point trajectories through the expiratory phases. The resulting average spatial error between the maximum phases was 1.25 mm for the 4DLTM and 1.44 mm for the CPP. The 4DLTM method was found to capture the long-range motion between 4DCT extremes with higher spatial accuracy (lesser spatial error).

J. Ehrhardt and associates [Ehrhardt, J. *et al.,* 2011] proposed a statistical modeling for 4D respiratory lung motion using diffeomorphic image registration. It was an approach to generate a mean motion model of the lung based on thoracic 4D computed tomography (CT) data of different patients to extend the motion modeling capabilities. The modeling process consisted of three steps: an intra-subject registration to generate subject-specific motion models, the generation of an average shape and intensity atlas of the lung as anatomical reference frame, and the registration of the subject-specific motion models to the atlas in order to build a statistical 4D mean motion model (4D-MMM). In all steps, a symmetric diffeomorphic nonlinear intensity-based registration method was employed. The model was evaluated by applying it for estimating respiratory motion of ten lung cancer patients. The prediction was evaluated with respect to landmark and tumor

motion, and the quantitative analysis resulted in a mean target registration error (T_{RE}) of 3.3±1.6 mm. With regard to lung tumor motion, it was shown that prediction accuracy is independent of tumor size and motion amplitude in the considered data set. The statistical respiratory motion model was found to be capable of providing valuable prior knowledge in many fields of applications. Authors also presented two examples of possible applications of the proposed method in radiation therapy and image guided diagnosis.

A.K. Sato and associates [Sato, A. K. *et al.,* 2011] proposed a method for registration of temporal sequences of coronal and sagittal MR images through respiratory patterns. This work discussed the determination of the breathing patterns in time sequence of images obtained from magnetic resonance (MR) and their use in the temporal registration of coronal and sagittal images. A time sequence of this intersection segment of orthogonal coronal and sagittal sequences were stacked, defining a two-dimension spatio-temporal (2DST) image. An interval-Hough transform algorithm was used to search for synchronized movements with the respiratory function. A greedy active contour algorithm would adjust small discrepancies originated by asynchronous movements in the respiratory patterns. The results of the proposed method in the form of synchronized sequences were compared with the pixel-by-pixel comparison method. The proposed method increased the number of registered pairs representing composed images and allowed an easy check of the breathing phase.

G. Xiong and associates [Xiong, G. *et al.*, 2012] proposed a method for tracking the motion trajectories of junction structures in 4D CT images of the lung. It was hailed as a novel method to detect a large collection of natural junction structures in the lung and use them as the reliable markers to track the

lung motion. The image intensities within a small region of interest surrounding the center were selected as its signature. Under the assumption of the cyclic motion, the trajectory was described by a closed B-spline curve and search for the control points by maximizing a metric of combined correlation coefficients. Local extremas were suppressed by improving the initial conditions using random walks from pair-wise optimizations. Several descriptors were also introduced to analyze the motion trajectories. The method was applied to 13 real 4D CT images. More than 700 junctions in each case were detected with an average positive predictive value of greater than 90%. The average tracking error between automated and manual tracking was in the sub-voxel category and smaller than the published results using the same set of data.

Yongbin Zhang and associates [Zhang, Y. *et al.*, 2013] proposed a method for modeling respiratory motion to reduce motion artifacts in 4D CT images. A patient-specific respiratory motion model was proposed, based on principal component analysis (PCA) of motion vectors obtained from deformable image registration, with the main goal of reducing image artifacts caused by irregular motion during 4D CT acquisition. Displacement vector fields relative to a reference phase were calculated using an in-house deformable image registration method. The authors then used PCA to decompose each of the displacement vector fields into linear combinations of principal motion bases. These projections were parameterized using a spline model to allow the reconstruction of the displacement vector fields at any given phase in a respiratory cycle. Finally, the displacement vector fields were used to deform the reference CT image to synthesize CT images at the selected phase with much reduced image artifacts. The initial large discrepancies across the landmark pairs were significantly

reduced after deformable registration, and the accuracy was similar to or better than that reported by state-of-the-art methods. The motion model was used to reduce irregular motion artifacts in the 4D CT images of three lung cancer patients. Visual assessment indicated that the proposed approach could reduce severe image artifacts. The proposed approach was found able to mitigate shape distortions of anatomy caused by irregular breathing motion during 4D CT acquisition.

B. Fuerst and associates [Fuerst, B. *et al.*, 2014] proposed a patient-specific biomechanical model for the prediction of lung motion from 4-d ct images. It was an approach to predict the deformation of the lungs and surrounding organs during respiration. Basically a computational model of the respiratory system, which comprises an anatomical model extracted from computed tomography (CT) images at end-expiration (EE), and a biomechanical model of the respiratory physiology, including the material behavior and interactions between organs. The method was then tested on five public datasets. Results showed that the model was able to predict the respiratory motion with an average landmark error of 3.40±1.0 mm over the entire respiratory cycle. The estimated 3-D lung motion may be constituted as an advanced 3-D surrogate for more accurate medical image reconstruction and patient respiratory analysis.

4.3 Method

4.3.1 Preparation

The dataset used comprised of a total (3×6)×10 i.e. 180 thoracic CT images across 10 subjects. There were 6 frames from a temporal thoracic image sequence each for every Anatomical Plane (AP) i.e. Axial (supine), Coronal and Sagittal for all

the 10 subjects acquired simultaneously with a gap of 0.1 second starting from time t= 0 to 0.6 seconds. All images were identified as $I_N^{AP}(x, y, t)$ where $\{N, t \in \mathbb{R}^+ | 1 \leq N \leq 10, 0.1 \leq t \leq 1\}$ and (x, y) are the coordinates in the Cartesian plane, t being the timestamp at which the particular frame/image was recorded, N would be the number assigned to the test subject and AP signifies the three anatomical planes of view i.e. Axial (a), Coronal (c) and Sagittal (s). So, the sixth subject's Coronal CT image acquired at t=0.3 sec would be identified as $I_6^c(x, y, 0.3)$. Samples of images used from all viewpoints and all subjects from timestamps 0.1 to 0.6 seconds are summarized in Table 4.1.

Table 4.1: Working database through all anatomical planes from t=0.1 to 0.6 sec

	Axial	Coronal	Sagittal
1	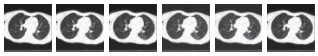	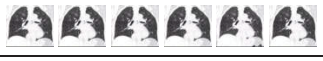	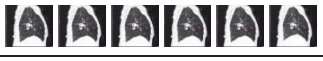
2	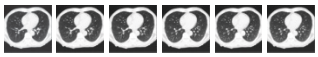		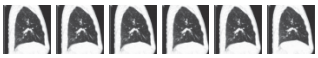
3	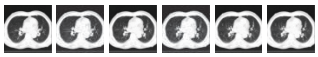		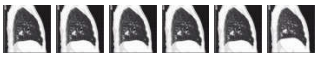
4	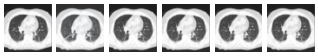	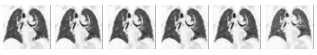	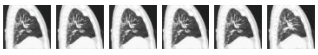
5	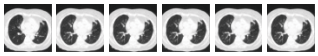	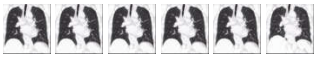	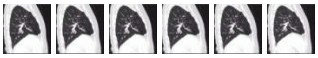
6	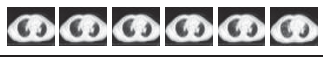		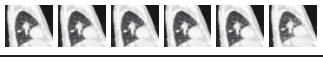
7			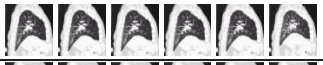
8			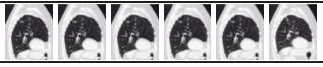
9	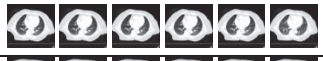		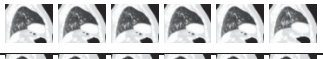
10		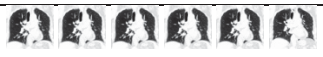	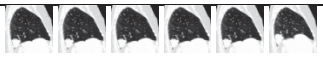

4.3.2 Proposed Methodology

The procedure acquired is as such that a temporal thoracic image sequence from time t=0.1 to 0.6 sec is taken such that first frame of the sequence is the full inhale frame and the last frame is full exhale frame. This paper uses the Speeded up

Robust Feature detector (SURF) [Bay, H. *et al.*, 2006, 2008] to obtain a feature set comprising of common feature points throughout the image sequence. It detects and describes the feature set irrespective of any scaling and /or rotation in the corresponding images. SURF provides better approximations in comparison to previously proposed schemes with respect to repeatability, distinctiveness, and robustness, yet can be computed and compared much faster than any other state of the art feature detector. These feature sets are then fed into the OFM estimation algorithm to identify the deformation path throughout the temporal sequence, be it peripheral or local.

Optical flow has been successfully applied to motion estimation of points/point clouds and other point set surface definitions over a temporal sequence [Sun, D. *et al.*, 2014]. It performs better than its contemporaries while tracing deformations that are realistic and guides the user in manipulation of real-world objects. It also allows the user to specify the deformations using either sets of points or line segments, the later useful for controlling curves and profiles present in the image. For each of these techniques, it provides simple closed-form solutions that yield fast deformations, which can be performed in real-time. The proposed methodology aims to track and estimate the deformations by tracking the transition of the interest points through the sequence from full inhale to full exhale frame. The overall process can be referred to in Figure 4.1.

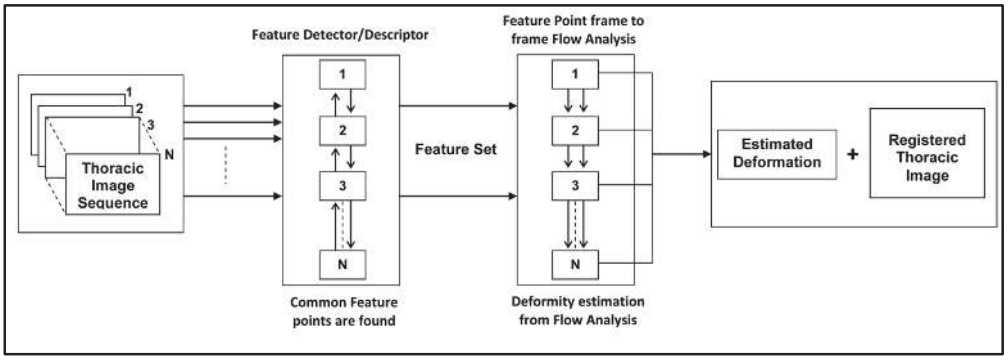

Figure 4.1: The proposed framework structure

A novel scale- and rotation-invariant detector and descriptor, has been coined as Speeded-Up Robust Features (SURF) by Herbert Bay et.al in 2006 [Bay, H. *et al.*, 2006] and 2008 [Bay, H. *et al.*, 2008]. It provides better approximations in comparison to previously proposed schemes with respect to repeatability, distinctiveness, and robustness, yet can be computed and compared much faster. Focus is on scale and in-plane rotation-invariant detection and descriptions. These seem to offer a good compromise between feature complexity and robustness to commonly occurring photometric deformations in thoracic images. Skewing, anisotropic scaling, and perspective effects are assumed to be second order effects, that are covered to some degree by the overall robustness of the descriptor. For guaranteed invariance to any scale changes the input thoracic images are analyzed at different scales. The detected interest points are provided with a rotation and scale-invariant descriptor. The detector is based on Hessian matrix based on its good performance in accuracy [Bay, H. *et al.*, 2008]. Blob-like structures are detected at locations with maximum determinant. In comparison to the Hessian-Laplace detector [Mikolajczyk, K. & Schmid, C., 2001] Hessian determinant is used for scale selection [Lindeberg, T., 1998].

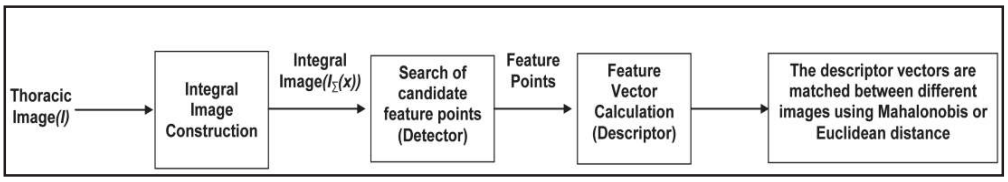

Figure 4.2: The working model of SURF

Given a point ***a*** = *(x, y)* in an image I_N^{AP}, the Hessian matrix $\hat{H}$***(a, σ)*** at scale σ is defined as follows

$$\hat{H}(a,\sigma) = \begin{bmatrix} L_{xx}(a,\sigma) & L_{xy}(a,\sigma) \\ L_{xy}(a,\sigma) & L_{yy}(a,\sigma) \end{bmatrix} \tag{4.1}$$

where $L_{xx}(a,\sigma)$ is the convolution of the Gaussian second derivative $\partial g(\sigma) / \partial a^2$ with the image I_N^{AP} at point ***a***, similarly for $L_{xy}(a,\sigma)$ and $L_{yy}(a,\sigma)$.

Though, Gaussians are optimal for scale-space analysis [Koenderink, J. J., 1984], they have to be made discrete and cropped in practice. This results in loss in repeatability of the detector for thoracic CT image rotations around odd multiples of π/4.

The SURF method consists of multiple stages to obtain relevant feature points from a sequence of thoracic images. The single SURF stages are (as shown in fig 4.2):

1. An integral image is constructed for each frame of the input thoracic image sequence, it allows for fast computation of box type convolution filters [Viola, P. & Jones, M., 2001]. This enables very few memory

accesses and hence results in drastic improvement in computational time [Cornelis, N. & Gool, L. V., 2008], which is especially crucial when we are dealing with a sequence of images. An integral image $I_{N\ \Sigma}^{AP}(a)$ at a location $\boldsymbol{a}= (x, y)^T$ represents the sum of all pixels in the input image I_N^{AP} within a rectangular region formed by the origin and $\boldsymbol{a}$

$$I_{N\ \Sigma}^{AP}(a) = \sum_{i=0}^{i\le x}\sum_{j=0}^{j\le y} I_N^{AP}(i,j) \tag{4.2}$$

2. Candidate feature points are searched by the creation of a Hessian scale-space pyramid (SURF detector). Approximation of the Hessian as a combination of box filters allows fast filtering. High contrast feature points are selected.
3. Feature vector is calculated (SURF descriptor) based on its characteristic direction to provide rotation invariance. Feature vector is normalized for immunity to changes in lighting conditions.
4. Matching of descriptor vectors between the thoracic image sequence frames using distance measures such as Mahalonobis distance and Euclidean distances etc.

Optical flow is the pattern of apparent motion of objects, surfaces, and edges in a visual scene caused by the relative motion between an observer (an eye or a camera) and the scene [Warren, D. H. & Strelow, E. R., 1985]. In recent times, the term optical flow has been co-opted by computer vision experts to incorporate related techniques from image processing and control of navigation, such as motion detection, object segmentation, time-to-contact information, focus of expansion calculations, luminance and motion compensated encoding and stereo

disparity measurement [Beauchemin, S. S. & Barron, J. L., 1995]. Sequences of ordered thoracic images allow the estimation of motion as either instantaneous image velocities or discrete image displacements [Aires, K. R. *et al.*, 2008]. Barron et.al provided a performance analysis of a number of optical flow techniques. It emphasizes the accuracy and density of measurements [Barron, J. L. et al., 1994].

Suppose we have a continuous thoracic image frame $I_N^{AP}(x, y, t)$; $f(x, y, t)$ refers to the gray-level of (x, y) at time t. It represents a dynamic thoracic image as a function of position and time. Few assumptions also work in hindsight:

- The detected feature point moves but does not actually change intensity.
- Feature point at location (x, y) in frame i is the feature point at (x+Δx, y+Δy) in frame *i+1* (detailed in figure 4.3).

For making computation simpler and quicker the real world three dimensional (3-D+time) objects are transferred to a (2-D+time) case. Then the thoracic image can be described by the 2-D dynamic brightness function of $I(x, y, t)$. Provided that in the neighbourhood of the feature point, change of brightness intensity does not happen in the motion field, following expression can be used:

$$I(x, y, t) = I(x + \delta x, y + \delta y, t + \delta t) \tag{4.3}$$

Taylor series is used for the right-hand side of the above equation, to obtain

$$I(x + \delta x, y + \delta y, t + \delta t) = I(x, y, t) + \frac{\partial I}{\partial x}\Delta x + \frac{\partial I}{\partial y}\Delta y + \frac{\partial I}{\partial t}\Delta t + \text{ Higher order terms} \tag{4.4}$$

From equations 4.3 and 4.4; neglecting the higher order terms,

$$\frac{\partial I}{\partial x}\Delta x + \frac{\partial I}{\partial y}\Delta y + \frac{\partial I}{\partial t}\Delta t = 0 \tag{4.5}$$

Dividing the terms in equation 4.5 by Δt on both sides (to get the equation in terms of x, y component velocity)

$$\frac{\partial I}{\partial x}{}^{\Delta x}\!/_{\Delta t} + \frac{\partial I}{\partial y}{}^{\Delta y}\!/_{\Delta t} + \frac{\partial I}{\partial t} = 0 \tag{4.6}$$

where ${}^{\Delta x}\!/_{\Delta t} = V_x$, ${}^{\Delta y}\!/_{\Delta t} = V_y$; thus,

$$\frac{\partial I}{\partial x}V_x + \frac{\partial I}{\partial y}V_y + \frac{\partial I}{\partial t} = 0 \tag{4.7}$$

Where V_x and V_y are the x and y components of velocity or optical flow of $I(x, y, t)$; $\frac{\partial I}{\partial x}$, $\frac{\partial I}{\partial y}$ and $\frac{\partial I}{\partial t}$ being the spatio-temporal derivatives of $I(x, y, t)$

$$I_x.v_x + I_y.v_y = -I_t \tag{4.8}$$

Vector representation being

$$\nabla I.\vec{v} == -I_t \tag{4.9}$$

Where ∇I is the spatial gradient of brightness intensity and $\vec{v}$ is the optical flow (velocity vector) of the previously detected feature points, I_t being the time derivative of the brightness intensity.

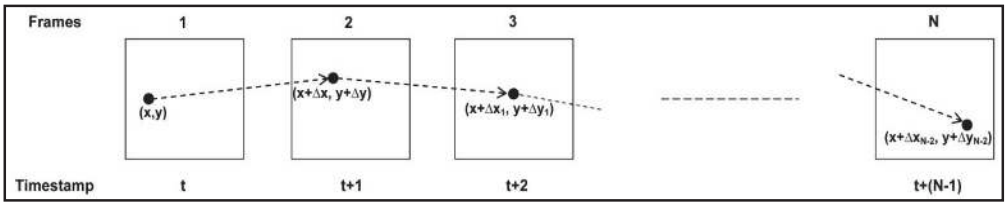

Figure 4.3: Flow of a common feature point (x, y) through a sequentially temporal thoracic image sequence with N frames, arrows indicate the changing velocity vector $\vec{v}$

4.4 Results and Discussion

The feature detector/descriptor implemented on the temporal image sequence gave out matching feature points among the six continuous frames of the thoracic continuous temporal image sequence $(0.1 \le t \le 0.6)$ where t is the timestamp of frames in the sequence for all Anatomical Positions (AP) with average translation values. The average translation between inter-frame durations for all common points 'P' from the initial to final frame:

$$d_{1avg} = \sum_{p_i=1}^{P} d_1 \Big/ P \quad , \quad d_{2avg} = \sum_{p_i=1}^{P} d_2 \Big/ P \quad \ldots\ldots\ldots\ldots\ldots\ldots \quad d_{N-1avg} = \sum_{p_i=1}^{P} d_{N-1} \Big/ P$$

Below figures (4.4 to 4.6) indicate the image registration process from the sequence for all test subjects through all three APs.

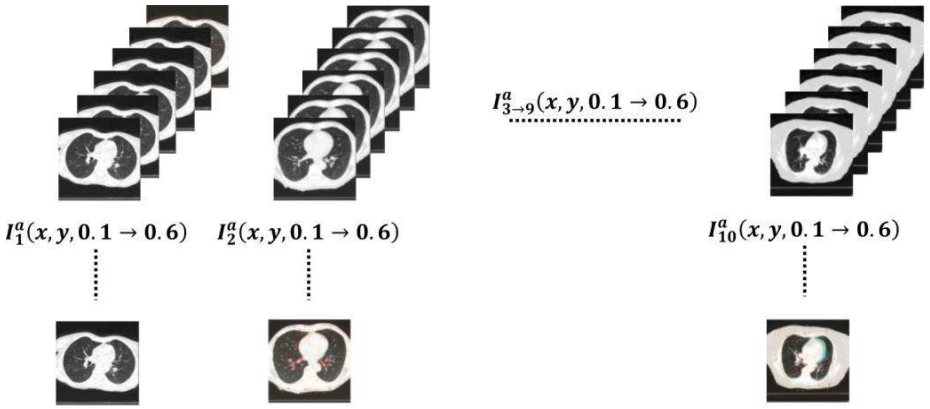

Figure 4.4: Image sequence frames and the registered image for all subjects-Axial

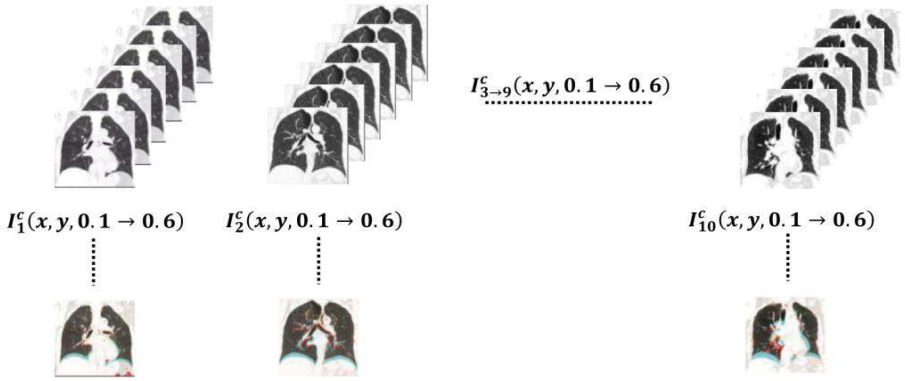

Figure 4.5: Image sequence frames and the registered image for all subjects- Coronal

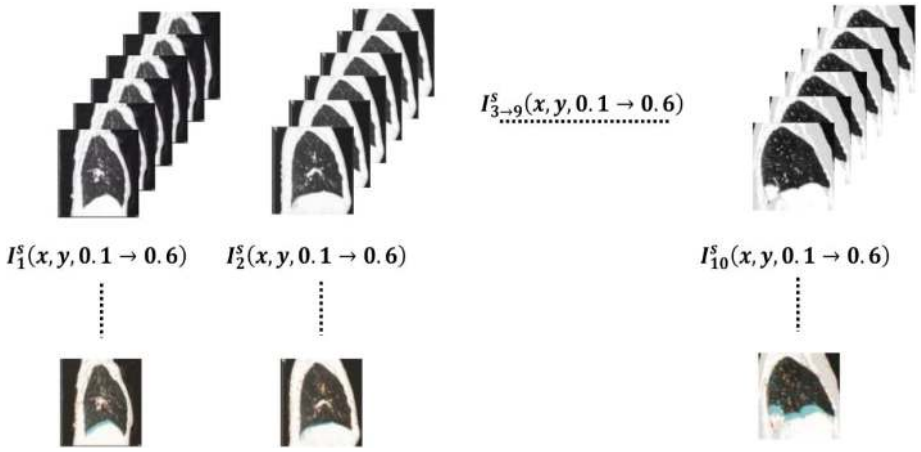

Figure 4.6: Image sequence frames and the registered image for all subjects- Sagittal

Though the proposed method was applied on all the subject data at hand, for representation purposes, subject 'case 5' sagittal AP data has been extensively used (as can be seen in fig. 4.7 to 4.11). The temporal sequence starting from t=0 to t=0.6 s is considered with a gap of 0.1 seconds between two consecutive frames in the sequence. So, frame 1 is the one acquired at t=0.1 and frame 6 is the one corresponding to t=0.6 s.

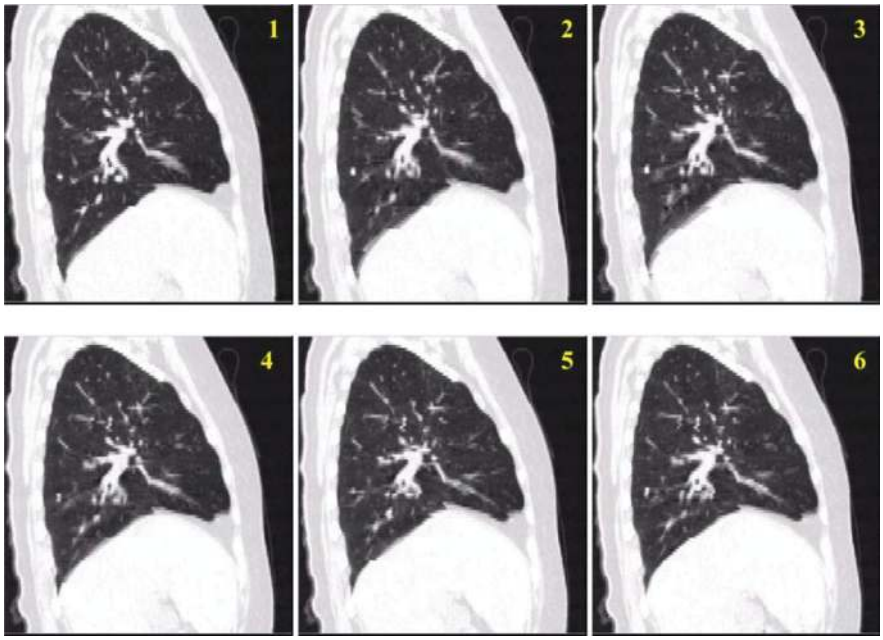

Figure 4.7: The test image temporal sequence (accordingly labelled). Subject 'case 5' Sagittal AP

The feature points are color coded with respect to the indices and IDs assigned to them throughout the process. The trails/tracks they leave after motion also exhibit the same color combination as assigned to respective feature points. There were 242 such feature points for the 'case 5' sagittal AP image sequence, the attributes of which are shown in the table E.1 (Appendix-E). Each of them had a track associated with them; these tracks have been labelled as Track_' point no' where the value of 'point no.' ranges from 0 to 241. Other attributes associated with each track included 'Track_Duration' which indicated the time in seconds for that respective track to finish and the point to reach its ultimate frame. 'Track_Start' is the stating time of every feature point trail/track; the value is '0' for all points, first frame being the reference frame for registration. 'Track_Stop' is the end time in seconds for respective tracks; values may be different for different feature points. 'Track_Displacement' is the net displacement from the point of origin for a feature point over the sequence. 'Track_(X,Y) Locations' are the points of

origin of the respective tracks. ‘Track_Min/Max/Mean Speeds’ are the minimum, maximum and mean speeds of the feature point trail/track for each point through the sequence. The displacement/translation obtained is inherently in pixel units. With the knowledge of PPI (pixel per inch) value of the respective images in question, the displacements can be converted into more tangible units. These average translations for all such feature points for all test subjects through all three APs are shown in tables 4.2 to 4.4. Their corresponding line plots for all 10 subjects are shown as figures 4.12 to 4.14 for easier comparative analysis over the complete breathing pattern. A corresponding false-color registered image representation is shown as fig. 4.9. Optical flow representation of the image sequence with respect to registered image along with a flow orientation scheme is shown in fig. 4.10. The optical flow at any point in the image can be decoded using the flow orientation scheme coding pinwheel given alongside. There was a rather large strip of single color found in the optical flow representation, which is synonymous with the false color representation in fig. 4.9. That is the location with maximum displacement/translation in the sequence and also of maximum deformation with respect to the reference frame.

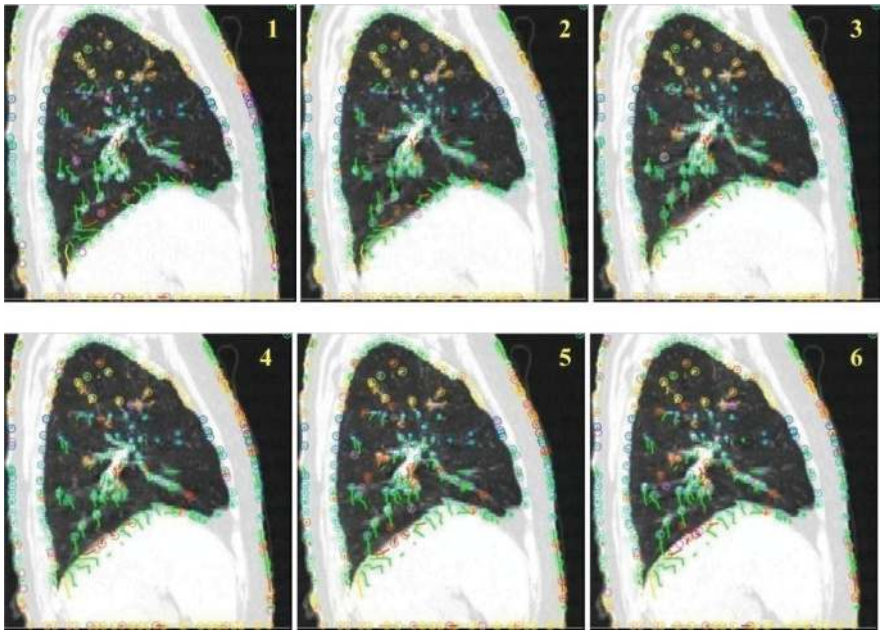

Figure 4.8: The color coded feature points and their colored trails showing the distinct paths for Sagittal AP 'case 5', frames are labeled in order of their temporal sequence

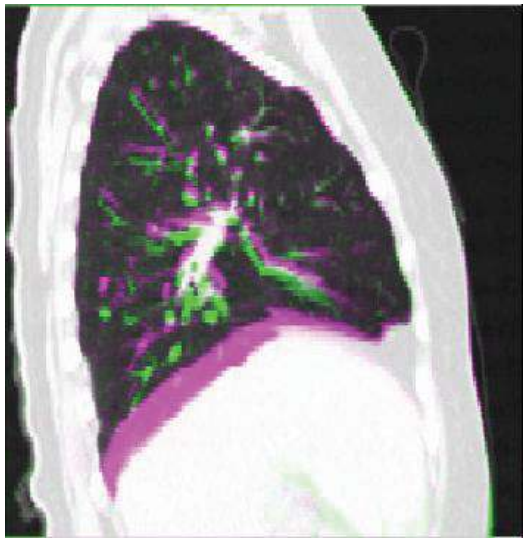

Figure 4.9: The registered image for the corresponding temporal sequence for subject 'case 5' Sagittal AP

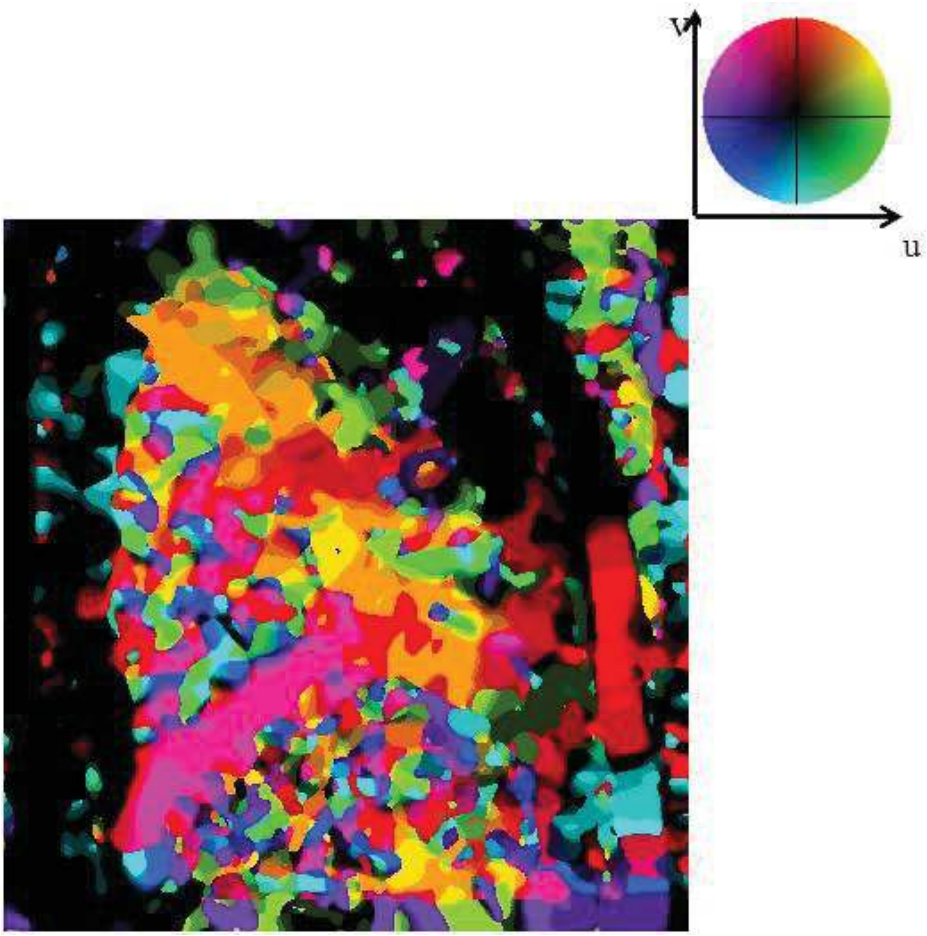

Figure 4.10: Color-coded Optic flow for subject 'case 5' sagittal AP with flow orientation scheme

Where fig. 4.10 indicated the optical flow orientation, magnitude of the optical flow is an important aspect that can be ignored when observing an image sequence over time. Fig. 4.11 represents the optical flow magnitude spread over the complete sequence with the first frame as reference. As can be seen from the magnitude scale provided alongside, the bigger red arrows indicate areas with higher magnitude of flow and larger deformations, while the blue and black arrows indicate areas lower optical flow magnitude and smaller deformations in respective locations.

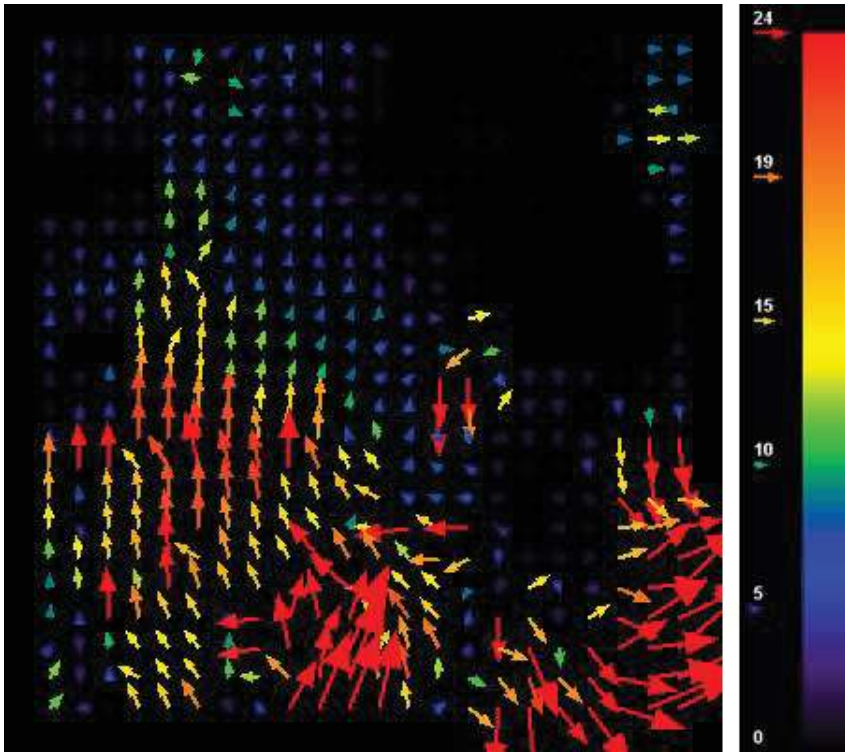

Figure 4.11: The overall image sequence optic flow with magnitude scale

Table 4.2: Average translations (in pixels) for all test subjects through Axial AP

AXIAL Average translation (pixels)										
slices	**case1**	**case2**	**case3**	**case4**	**case5**	**case6**	**case7**	**case8**	**case9**	**case10**
1	0.047	0.000	0.050	0.128	0.103	0.122	0.105	0.081	0.148	0.235
2	0.074	0.054	0.212	0.263	0.220	0.192	0.173	0.176	0.157	0.235
3	0.121	0.090	0.078	0.260	0.217	0.232	0.160	0.197	0.154	0.491
4	0.236	0.041	0.077	0.120	0.335	0.224	0.123	0.236	0.273	0.550
5	0.165	0.087	0.235	0.054	0.229	0.277	0.175	0.227	0.346	0.415

Table 4.3: Average translations (in pixels) for all test subjects through Coronal AP

CORONAL Average translation (pixels)										
slices	**case1**	**case2**	**case3**	**case4**	**case5**	**case6**	**case7**	**case8**	**case9**	**case10**
1	0.049	0.241	0.090	0.337	0.090	0.272	0.413	0.316	0.705	0.389
2	0.257	0.445	0.284	0.441	0.545	0.444	0.574	0.563	1.515	0.587
3	0.544	0.451	0.490	0.436	0.574	0.434	0.547	0.600	1.541	2.594
4	0.555	0.396	0.443	0.414	0.617	0.458	0.522	0.700	1.508	0.707
5	0.361	0.381	0.529	0.495	0.682	0.532	0.503	0.645	1.432	0.586

Table 4.4: Average translations (in pixels) for all test subjects through Sagittal AP

SAGITTAL Average translation (pixels)										
slices	**case1**	**case2**	**case3**	**case4**	**case5**	**case6**	**case7**	**case8**	**case9**	**case10**
1	0.056	0.102	0.033	0.198	0.022	0.218	0.283	0.387	0.318	0.348
2	0.067	0.038	0.031	0.225	0.081	0.515	0.451	0.603	0.410	0.439
3	0.229	0.144	0.036	0.184	0.131	0.511	0.504	0.639	0.336	0.476
4	0.120	0.125	0.041	0.228	0.092	0.483	0.574	0.666	0.374	0.521
5	0.131	0.042	0.027	0.237	0.079	0.545	0.504	0.659	0.326	0.505

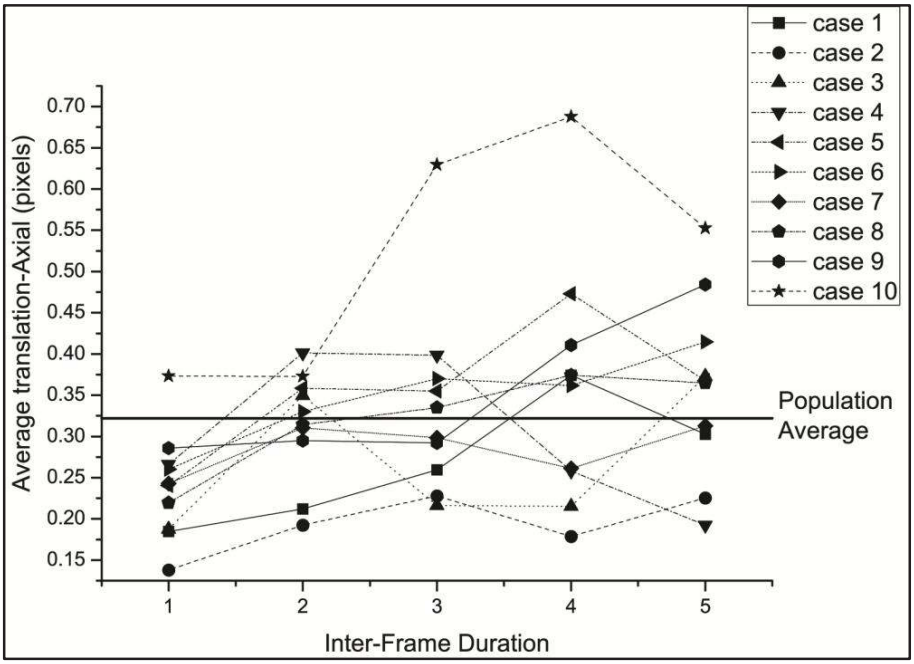

Figure 4.12: Average displacement for all subjects in Axial AP

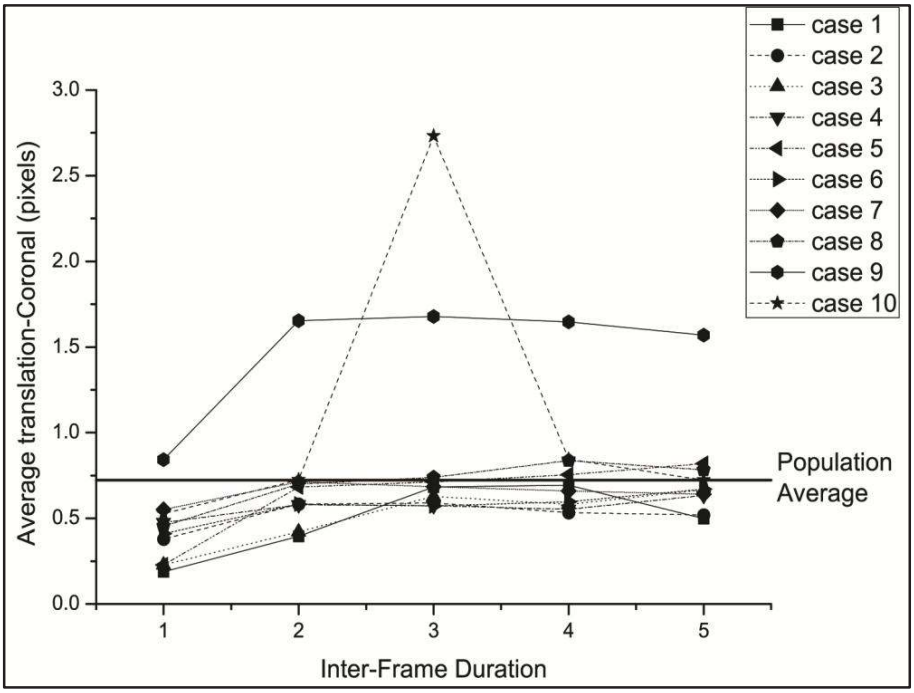

Figure 4.13: Average displacement for all subjects in Coronal AP

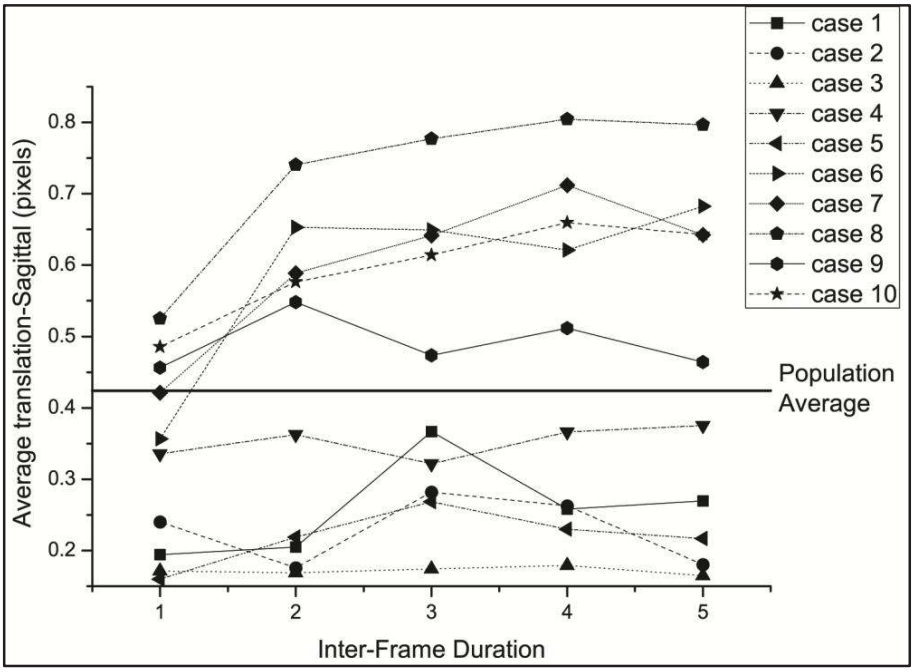

Figure 4.14: Average displacement for all subjects in Sagittal AP

As we can see in fig. 4.12, the axial translations were recorded highest for subject 'case 10' and the lowest corresponding values were for 'case 2'. The average value for 'case 10' was recorded at 0.3851 pixels, which was way above the population average of 0.184 shown by a line across the plot. In case of coronal AP as can be seen in fig. 4.13, the biggest deformations throughout the sequence are exhibited by the subjects 'case 10' and 'case 9' at 2.594 and 1.54 pixels respectively. The population average in this case being 0.5847 marked by a straight line in the corresponding plot. Though apart from 'case 10' only 'case 9'exhibited bigger deviations than the average value, the change in deformation with respect to inter-frame durations was more or less constant; on the other hand 'case 10' exhibited enormous shift from the average value while transitioning from 3rd frame to 4th frame. Looking at fig. 4.14 for the sagittal AP, all subjects though a bit above and below the average maintain an almost constant rate of

change in the deformations and do not exactly exhibit any erratic patterns through the observed full inhale to exhale process. After having a comprehensive look at all subjects' deformation pattern data through axial, coronal and sagittal APs collectively, it was inferred that subject 'case 10' singled out as the only one with maximum deformation. This analysis indicates anomalous breathing patterns from the aforementioned subject among the considered consensus average.

4.5 Conclusion

A framework has been presented showing how to use a feature point set generated using a Hessian-matrix based feature detector and Haar wavelets based descriptor such as SURF through a motion estimation technique such as OFM tracking for deformable image transformations in medical images such as the thoracic 'pectus excavatum' [Haller, J. A. et al., 1987; Kim, H. C. et al., 2010] full exhale and full inhale used in this work. This conclusion is of high clinical relevance from a diagnostic point of view as well; the artifacts and position uncertainties due to uneven breathing patterns which hamper the image guided clinical interventions can be corrected to a point where there influence on the actual data and the diagnostics based on them is brought down to the least.

This work can be looked upon as an automatic way of deformable image registration for high contrast medical images using landmark (control) points. Although the proposed methodology provides with a fast and accurate way of DIR for medical images and thus an account of deformity in the thoracic periphery, there is much scope for improvement in the overall process. One way this can be achieved in future is by modifying the SURF and/or the Motion estimation procedure involved in the process. Another way is to improve and enhance the quality as well as the quantity of the database used. Also, the aforementioned

procedure can provide better results if applied for a different human anatomy altogether.

However diligently and accurately it may have been done, there might still be some scope of improvement and betterment in the methodology and also in its presentation. The search and pursuit of better methods for deformable medical image registration is still on.